Expanding the measurement capabilities of the mARC II arc-jet to map the operating envelope for high-enthalpy air flows

Jocelino Rodrigues*
NASA Postdoctoral Program at NASA Ames Research Center, Moffett Field, California, 94035, USA

Megan E. MacDonald†, Magnus A. Haw‡, Ramon Martinez§, and Daniel Philippidis¶
NASA Ames Research Center, Moffett Field, California, 94035, USA

Sebastian Colom‖
AMA Inc. at NASA Ames Research Center, Moffett Field, California, 94035, USA

Ryan Chung** and Joe Hartman††
Sierra Lobo Inc. at NASA Ames Research Center, Moffett Field, California, 94035, USA

The mARC II is a 30 kW arc-jet facility at NASA Ames Research Center developed to produce high-enthalpy flows for low-cost technology development purposes. In this work, we introduce new measurement capabilities following the latest facility upgrades and begin characterizing the operating envelope for the two-disk arc-heater configuration with air as the working gas. The lower bound of the envelope corresponds to the lowest set current and the farthest sensor distance from the nozzle ($I_{\text{set}} = 40$ A, $z = 69$ mm), while the upper bound corresponds to the highest current and closest sensor distance ($I_{\text{set}} = 200$ A, $z = 2$ mm). Stagnation point heat flux was measured using a water-cooled Gardon gauge (⌀4.76 mm, 3/16" hemispherical), with values ranging from $15 \leq \dot{q}_0 \leq 900$ W/cm^2. Stagnation pressure was measured using a water-cooled Pitot probe (⌀4.76 mm, 3/16" hemispherical), with values ranging from $18 \leq p_0 \leq 1100$ Pa. The upgraded vacuum system is demonstrated to significantly extend the lower end of the operating envelope of the mARC II. Additionally, measurements of bulk enthalpy ($3 \leq \bar{h} \leq 13$ MJ/kg) and stagnation enthalpy ($4 \leq h_0 \leq 34$ MJ/kg) demonstrate the mARC II facility's high-enthalpy capabilities. Completion of the operating envelope characterization is ongoing in tandem with the development of complementary diagnostic capabilities and numerical simulations.

Nomenclature

Acronyms

IST = Integrated Systems Testing
mARC II = miniature Arc-jet Research Chamber (second-generation)
NASA = National Aeronautics and Space Administration
TRL = Technology Readiness Level

Greek symbols

Δ = change in value
γ = heat capacity ratio
σ = standard deviation

---

[*] NPP Research Fellow, Thermophysics Facilities Branch, Entry Systems & Technology Division (jocelino.rodrigues@nasa.gov).
[†] Aerospace Engineer, Thermophysics Facilities Branch, Entry Systems & Technology Division (megan.e.macdonald@nasa.gov).
[‡] Plasma Physicist, Thermal Protection Materials Branch, Entry Systems & Technology Division.
[§] EAST and mARC Facilities Manager, Thermophysics Facilities Branch, Entry Systems & Technology Division.
[¶] Aerospace Engineer, Thermophysics Facilities Branch, Entry Systems & Technology Division.
[‖] Research Engineer, Thermal Protection Materials Branch, Entry Systems & Technology Division.
[**] Test Engineer, Thermophysics Facilities Branch, Entry Systems & Technology Division.
[††] Senior Engineering Consultant, Thermophysics Facilities Branch, Entry Systems & Technology Division.

Roman symbols

c_p = isobaric specific heat
h = enthalpy
I = current
K = heat transfer gas constant
M = Mach number
$\dot{m}$ = mass flow rate
p = pressure
P = power
$\dot{q}$ = heat flux
r = radius
t = time
T = temperature
V = voltage
z = axial distance from nozzle exit plane

Superscripts

$\bar{(\cdot)}$ = average or bulk value

I. Introduction

Small-scale arc-jet facilities have been steadily gaining popularity in the aerospace community, both in industry and in academia. Their low-cost allows for both the systematic study of high-enthalpy flow physics and the high-throughput testing for material screening.

The second-generation miniature arc-jet research chamber (mARC II) is the culmination of nearly two decades of development at NASA Ames Research Center aimed at addressing the need for an in-house facility to support the advancement of low-TRL aerothermal technologies for atmospheric entry applications [1–12]. The mARC II facility aims to enable low-TRL technologies to mature sufficiently before they are tested in larger facilities. This approach provides opportunities for innovations that might otherwise be overlooked and accelerates the development process by offering a means to obtain quick and reliable data.

In 2024, the mARC II underwent significant upgrades, including modifications to the vacuum system to maintain underexpanded flow during test conditions [13]. As part of the Integrated Systems Testing (IST), check-out runs were conducted, and the resulting data confirmed that the upgraded vacuum system successfully sustained underexpanded conditions. Stagnation point heat flux measurements, obtained using a water-cooled Gardon gauge (⌀4.76 mm, 3/16" hemispherical), showed that lower test box pressures led to reduced stagnation point heat flux for the same arc-heater conditions, compared to data collected before the upgrades. These results indicated that the upgrades effectively expanded the lower end of the heat flux operating regime.

In this work, we expand the mARC II's measurement capabilities to characterize the facility's operating envelope for air flows, including radial heat flux profiles, stagnation pressure, and stagnation enthalpy. Additionally, we introduce spectrally-filtered, high-resolution video imaging of the freestream region to capture flow characteristics before and during sensor dwell. In §II, we describe the methods used in this study, and in §III we present and discuss the results obtained.

II. Methods

In this section, we describe the arc-jet facility and instrumentation used. We also review the formulations used to estimate flow enthalpy and freestream Mach number.

A. Experimental setup

1. Arc-heater

The mARC II is a 30 kW segmented constricted arc-heater (Fig. 1a). The arc-heater uses a Hypertherm MAX200 plasma cutter for power supply and gas flow management, both of which are manually controlled by certified personnel. In this work, arc-heater was used with two constrictor disks (one of which has a pressure tap), a cathode, an anode, and a convergent-divergent nozzle (⌀5.56 mm throat and ⌀18.67 mm exit). The cathode is housed inside the Hypertherm torch body and integrated inside the arc-heater. Two active water-cooling circuits are utilized: one which cools the cathode torch, and the another which cools the arc column, nozzle, test box walls, diffuser, and heat exchanger. A coolant mixture consisting of propylene glycol (30%) and deionized water (70%) is used in the cathode torch coolant circuit. Deionized water with electrical conductivity of 0.6–2.0 µS is used for the latter cooling circuit.

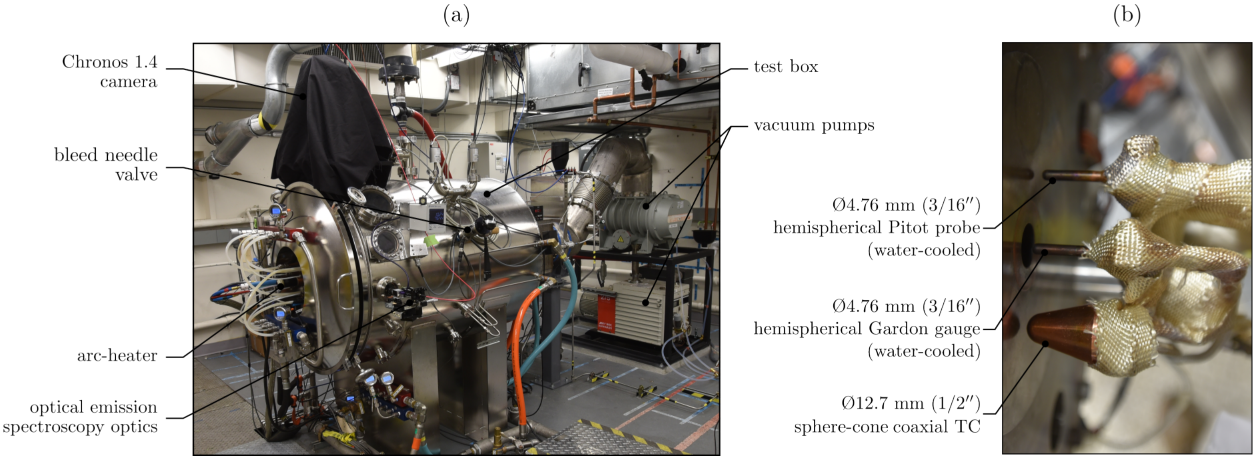

Fig. 1 Experimental setup: (a) upgraded second-generation miniature Arc-jet Research Chamber (mARC II) (b) trident (three-mount) sweep arm with two heat flux sensors and one stagnation pressure sensor at z = 2 mm from the nozzle exit plane (for runs 5 and 6 – see Table 2).

2. Vacuum system

The mARC II recently underwent significant upgrades in the vacuum pump system through the addition of an Edwards EH4200 mechanical booster pump which was coupled to the existing Edwards E2M275 two-stage direct drive rotary vane pump. In addition, a water-cooled diffuser and a water-cooled heat exchanger were added to the facility. These upgrades enable the mARC II to reach medium (or *fine*) vacuum conditions (2–5 Pa) before the start of each run and to maintain constant pressure after the addition of air and arc-on (≤22 Pa in this work – see Table 2). As a result of the arc column pressures being on the order of 10^4 kPa and the nozzle area ratio being $A/A^* \simeq 11.3$, the nozzle flow is underexpanded [14]. For more details on the mARC II arc-heater and the recent facility upgrades, please refer to the work of MacDonald et al. [8, 9, 11] and Rodrigues et al. [13].

3. Instrumentation

Measurements of arc-jet facility data, such as arc current I_{arc}, arc voltage V_{arc}, air mass flow rate $\dot{m}$, arc column pressure $\bar{p}_{\mathrm{col}}$, test box pressure p_∞, cooling water flow rate $\dot{m}_{\mathrm{w}}$, and cooling water temperature change ΔT_{w} were acquired for all the runs at a sampling rate of 20 Hz. A trident (three-mount) sweep arm is used to house the freestream flow measurement sensors (Fig. 1b) [11]. It is wrapped using high-temperature Refrasil cloth (use limit of approximately 1000 °C) to thermally insulate it from the high-temperature flow.

The distance of the sweep arm from the nozzle is manually adjustable. In this work, the sensors are positioned at z = 2 mm or z = 69 mm from the nozzle exit plane. A servo motor (Clearpath CPM-SCSK-2311S-ELSA) is used to provide reliable sweeping performance of the sensors into the high-speed plasma flow [11]. A data acquisition hardware package separate to that of the facility data system is used to simultaneously acquire data from the sensors mounted on the trident sweep arm, as well as other thermocouple signals. This separate hardware package includes a LabJack T7-Pro data acquisition board, a CB37 terminal board, and several LabJack Tick-InAmp (LJTIA) pre-conditioning modules providing up to 252X amplification to low-level signals at 2 GΩ impedance. The LabJack T7-Pro enables fast (up to 8 kHz) high-fidelity (16 bit) data sampling.

Table 1 lists the key instruments used to make measurements in this work. In the next subsections, we provide additional details on the three sensors used in the trident sweep arm mounts.

3.1. Stagnation point heat flux: water-cooled Gardon gauge (⌀4.76 mm, 3/16" hemispherical)

Stagnation point heat flux measurements are made using a water-cooled Gardon gauge with a ⌀4.76 mm (3/16") hemispherical copper body (Medtherm 12-3000-1.0-6-72-21631T). A high-pressure water cooling system is employed to keep the Gardon gauge within acceptable temperatures [11]. The Gardon gauge is the mARC II reference stagnation point heat flux sensor and is dwelled for 1 s at each condition. This dwell time was selected because it allows for the measurement of steady-state heat flux while minimizing unnecessary exposure to the high-temperature freestream flow.

Table 1 List of relevant instrumentation used during mARC II operation. Measurement capabilities added since the facility upgrades are colored.

Measurement	*Symbol*	*Unit*	*Instrument*
Arc column static pressure	p_{col}	[kPa]	Setra Model 730 capacitance manometer
Arc current	I_{arc}	[A]	Ohio Semitronics CTL-401S/300 current transducer (x2) Ohio Semitronics CTA 201H signal conditioner (x2)
Arc voltage	V_{arc}	[V]	Ohio Semitronics VT7-007E-11-TP voltage transducer
Heat flux (stagnation point)	$\dot{q}_{0,\text{G}}$	[W/cm^2]	Medtherm water-cooled Gardon gauge (⌀4.76 mm hemispherical)
Heat flux (radial sweep)	$\dot{q}_{\text{C}}$	[W/cm^2]	Medtherm/AEDC coaxial TC calorimeter (⌀12.7 mm, 15° sphere-cone)
Stagnation point pressure	p_0	[Pa]	Medtherm water-cooled Pitot probe (⌀4.76 mm hemispherical)
Supply air mass flow rate	$\dot{m}$	[g/s]	Sage SIP-030-DC24-AIR thermal flow meter
Test box static pressure	p_∞	[Pa]	Inficon SKY CDG025D capacitance manometer (1000 torr) Inficon SKY CDG025D capacitance manometer (10 torr)
Water flow rate	$\dot{m}_{\text{w}}$	[g/s]	Omega FTB795/FTB796 turbine flow meter
Water/glycol coolant temp. change	ΔT_{cool}	[K]	Osensa PRB-SW1 fiber optic temperature sensor (x2) FTX-300-LUX+ fiber optic temperature transmitter
Water temp. change	ΔT_{w}	[K]	E & C Co., Thermoducer 8 (17 Ω, 3000 psi)

3.2. Radial heat flux profile: coaxial thermocouple heat flux gauge (⌀12.7 mm, 15° sphere-cone)

A coaxial thermocouple calorimeter (Medtherm TCS–099–T–0.4–Cu–600–11565) is used to quantify the heat flux profile. This is a Type T coaxial thermocouple which has been press-fit into a ⌀12.7 mm sphere-cone geometry with a 15° taper that was manufactured from oxygen-free, high-conductivity copper (OHFC) [15, 16]. The signal output is processed using the International Temperature Scale of 1990 (ITS-90) inverse polynomials [17]. The sensor has a temperature limit of 350 °C and a response time of approximately 1 μs. The coaxial calorimeter was swept through the freestream flow at 50 rpm (linear sweep speed of 66.5 cm/s). We correct for two-dimensional effects seen in these types of calorimeters by employing a tridiagonal matrix algorithm that solves the heat conduction equations in the radial co-ordinate system [18].

3.3. Stagnation pressure: water-cooled Pitot probe (⌀4.76 mm hemispherical)

A water-cooled Pitot probe with a ⌀4.76 mm (3/16") hemispherical copper body (Medtherm 12–PP–1.0–6–10–50553) is used with a pressure transducer (Endevco 8530C-15) to measure the stagnation pressure. The transducer has a quoted uncertainty of $\sigma = \pm 0.1\%$FSO (FSO = 103,420 Pa) which equates to $\sigma = \pm 103.42$ Pa (68.3% CI).

During the tests conducted for this work, the pressure transducer demonstrated temperature sensitivity, which was particularly evident in the lower region of the operating regime. An extensive in-situ calibration of the Pitot probe pressure was performed across its full operating range, accounting for transducer temperature. This calibration led to the development of an algorithm that corrects for thermal offset shift and sensitivity. The first version of this algorithm is used in this work, and details of the calibration process and algorithm will be provided in a future publication. The Pitot probe is dwelled for either 1 s (for the $I_{\text{set}} = 200$ A condition) or 2 s (for the $I_{\text{set}} = 40$ A condition). The selection of dwell time represented a compromise between allowing sufficient time for the pressure line to fill up and reach steady-state while minimizing heating of the transducer due to its temperature sensitivity.

B. Freestream flow and sensor imaging

Imaging capabilities have been improved since the last mARC II publication [13]. In this work, we present preliminary spectrally-filtered images from a monochrome Chronos 1.4 high-speed camera (32 GB, 1.4 Gpx/s, 1.3 MP, 12-bit, Kron Technologies). The Chronos 1.4 camera was used to visualize the freestream flow and how it changes once the sensors are swept and dwelled in the flow through the top window of the mARC II test box (⌀147.5 mm, thickness of 12.5 mm, fused silica). The camera and window are covered with a blackout cloth during each run to minimize the impact of external light on the collected data (Fig. 1a). The camera's standard IR cut-off filter was removed and a Navitar Zoom 7000 macro lens system was attached (without the detachable close-up lens). A lens tube was used in between the camera and the Zoom 7000 to house a bandpass filter in the near-infrared (NIR) spectrum (780±5 nm, ThorLabs FBH780-10). This was chosen to visualize the neutral atomic oxygen O I triplet at 777 nm [19, 20]. Video was recorded at 30 fps and each frame was exported as a Tagged Image File Format (TIFF) Raw file with linear brightness encoding. A resolution of 1280×1024 px was used, yielding a field of view of 85×68 mm after spatial calibration (15.06 px/mm, pixel length of 66.41 µm).

C. Freestream enthalpy

Two key parameters to describe arc-jet performance are the bulk and stagnation enthalpies. In this section, we describe how both freestream enthalpy properties are quantified using data obtained from experimental measurements.

1. Bulk flow enthalpy $\bar{h}$

Bulk enthalpy $\bar{h}$ is estimated from the arc power P_{arc} and the power lost in the arc-heater cooling circuits ΔP_{cool} using the ASTM E341–08 standard for energy balance:

$$\bar{h} = \frac{P_{\text{arc}} - \Delta P_{\text{cool}}}{\dot{m}} = \frac{P_{\text{arc}} - \Delta P_{\text{cathode}} - (\Delta P_{\text{anode}} + \Delta P_{\text{disks}} + \Delta P_{\text{nozzle}})}{\dot{m}} \,, \tag{1}$$

where:

$$P_{\text{arc}} = I_{\text{arc}} V_{\text{arc}} \,, \qquad \Delta P_{\text{cathode}} = \dot{m}_{\text{cool}} c_{p,\text{cool}} \Delta T_{\text{cool}} \,, \qquad \Delta P_{\text{anode}} + \Delta P_{\text{disks}} + \Delta P_{\text{nozzle}} = \dot{m}_{\text{w}} c_{p,\text{w}} \Delta T_{\text{w}} \,, \tag{2a-c}$$

and I_{arc} is the arc current, V_{arc} is the arc voltage, $\dot{m}$ is the mass flow rate of air, $\dot{m}_{\text{w}}$ is the cooling water mass flow rate, ΔT_{w} is the temperature difference between the water supply and return lines, and $c_{p,\text{w}} = 4180$ J/kg-K is the isobaric specific heat capacity of water [21, 22]. In Eq. (2)c, we assume heat loss along the lines are negligible.

In our previous work, the cathode losses $\Delta P_{\text{cathode}}$ were assumed to be negligible due to the cathode surface area being small ($\varnothing < 1$ mm) [13]. In this present work, we quantify these losses. A known coolant mixture of propylene glycol (30%) and deionized water (70%) is used in the MAX200 power supply coolant tank (11 L capacity). This mixture has an isobaric specific heat capacity of $c_{p,\text{cool}} = 3960$ J/kg-K which varies as a function of temperature [23–25]. The coolant flow rate was measured to be $\dot{m}_{\text{cool}} \simeq 0.073$ kg/s. The coolant temperature difference ΔT_{cool} is measured using two optical fiber sensors (Osensa PRB-SW1). One is attached to a brass fitting on the coolant supply line and the other to a brass fitting on the coolant return line. A signal conditioner (Osensa FTX-300-LUX+) is used to emit light pulses to each sensor and measure the subsequent phosphor decays to obtain temperature readings. The sensors were calibrated using a precision temperature calibration bath (Fluke 7321).

2. Stagnation enthalpy h_0

The stagnation enthalpy h_0 can be calculated according to the ASTM E637–22 standard, with experimental measurements for stagnation point heat flux $\dot{q}_0$ and stagnation pressure p_0 applied to a semi-empirical formulation:

$$h_0 = \left(\sqrt{\frac{r_{\text{N,hemi}}}{K^2}} \right) \frac{\dot{q}_{0,\text{hemi}}}{\sqrt{p_0}} + h_{\text{w}} \,, \tag{3}$$

where $K = 3.905 \times 10^{-4}$ kg N^{-5} m^{-5} s^{-1} is the heat transfer gas constant for air, $r_{\text{N,hemi}}$ is the nose radius of a hemispherical calorimeter, and h_{w} is the wall enthalpy [26–33]. The Gardon gauge heat flux is used for $\dot{q}_{0,\text{hemi}}$ in this equation, such that $r_{\text{N,hemi}} = 2.36$ mm. As a result of being computed from stagnation heat flux and pressure measurements, this flow property has also been referred to as *inferred* stagnation enthalpy [34]. Since the Gardon gauge is water-cooled, the wall enthalpy is considered negligible relative to the stagnation enthalpy, such that $h_{\text{w}} = 0$.

D. Freestream Mach number

For an ideal gas, the Rayleigh-Pitot formula can be used to estimate the freestream Mach number M_∞ upstream of the shock that is produced by the insertion of the Pitot probe in the supersonic plasma flow:

$$\frac{p_0}{p_\infty} = \left(\frac{(\gamma_\infty + 1) M_\infty^2}{M_\infty^2 (\gamma - 1) + 2} \right)^{\frac{\gamma_\infty}{\gamma_\infty - 1}} \left(\frac{\gamma_\infty + 1}{2\gamma_\infty M_\infty^2 - (\gamma_\infty - 1)} \right)^{\frac{1}{\gamma_\infty - 1}} \,, \tag{4}$$

where p_0 is the stagnation pressure measured by the Pitot probe, p_∞ is the static pressure in the test box, and γ_∞ is the freestream specific heat capacity ratio [35, 36].

III. Results

A. Data overview

Table 2 summarizes the operating envelope results presented in this study. For the arc-heater, the table includes the average air mass flow rate $\bar{\dot{m}}$, total arc current $\bar{I}_{\mathrm{arc}}$, arc voltage $\bar{V}_{\mathrm{arc}}$, and arc power $\bar{P}_{\mathrm{arc}}$. The operating envelope results encompass several key parameters: the average steady-state test box pressure $\bar{p}_\infty$, the freestream Mach number upstream of the Pitot probe $\bar{M}_\infty$ (estimated via the Pitot-Raleigh formula described in §II.D), and the distance from the sensor tips to the nozzle exit plane z.

The outputs from the trident sweep arm instrumentation are also presented. These include the peak stagnation point heat flux $\bar{\dot{q}}_{0,\mathrm{C}}$ measured by coaxial thermocouple calorimeter (⌀12.7 mm, 1/2" sphere-cone) swept at a linear speed of 66.5 cm/s, the average stagnation point heat flux $\bar{\dot{q}}_{0,\mathrm{G}}$ measured by a water-cooled Gardon gauge (⌀4.76 mm, 3/16" hemispherical) during a 1-second dwell, and the average stagnation pressure $\bar{p}_0$ measured by a water-cooled Pitot probe (⌀4.76 mm, 3/16" hemispherical) during either a 1- or 2-second dwell. Given that the coaxial sensor and the Gardon gauge have distinct geometries – both in shape and size – we would expect the sensors to yield different heat flux measurements, a trend that is confirmed by the data. Methods to correct for geometry and directly compare measured heat fluxes from calorimeters of varying sizes and shapes are under development and will be proposed in future studies. Lastly, stagnation enthalpy h_0, computed using the ASTM E637–22 standard, and bulk flow enthalpy $\bar{h}$, estimated using the ASTM E341–08 standard, are reported. The centerline-to-bulk enthalpy ratio $h_0/\bar{h}$ is included for reference.

Figure 2 shows the time-resolved output signals from the sensors mounted on the sweep arm during run 6, from which both peak and average results are derived. The figure includes both the raw and filtered signals, with the latter used for the final outputs. High-frequency noise has been removed using a low-pass Butterworth filter, with a cut-off frequency selected to preserve the rise time of the raw signal. The coaxial temperature signal presented in Fig. 2a is input into a tridiagonal matrix algorithm to solve a heat conduction equation and calculate the heat flux, as described in §II.A.3. The resulting heat fluxes from the coaxial sensor are presented in §III.C.

B. Freestream enthalpy *h*

In this study, the mARC II facility operated with air as the working gas. The corresponding flow enthalpy and stagnation properties were analyzed, as shown in Fig. 3.

Figure 3a compares stagnation enthalpy h_0 with bulk flow enthalpy $\bar{h}$. The stagnation point heat flux $\dot{q}_0$ used to calculate stagnation enthalpy was measured by the Gardon gauge, which serves as the reference heat flux gauge. As expected, stagnation enthalpy exceeds bulk enthalpy in all cases, as it includes both static and kinetic energy contributions. In high-enthalpy flows, the freestream contains significant kinetic energy, which is converted into internal energy

Table 2 Summary of outputs: mARC II configuration with two constrictor disks using air as the working gas.

Run	Arc-heater					Operating envelope (air, two constrictor disks)								
	$\bar{\dot{m}}$	$\bar{I}_{\mathrm{arc}}$	$\bar{V}_{\mathrm{arc}}$	$\bar{P}_{\mathrm{arc}}$	$\bar{p}_{\mathrm{col}}$	$\bar{p}_\infty$	$\bar{M}_\infty$	z	$\bar{\dot{q}}_{0,\mathrm{C}}$	$\bar{\dot{q}}_{0,\mathrm{G}}$	$\bar{p}_0$	h_0	$\bar{h}$	$h_0/\bar{h}$
	[g/s]	[A]	[V]	[kW]	[kPa]	[Pa]	[–]	[mm]	[W/cm^2]		[Pa]	[MJ/kg]		[–]
1	0.13	42	91	3.8	7.4	14	1.9	69	10	15	18	4.2	3.0	1.4
2	0.14	42	97	4.0	8.1	15	1.8	69	11	17	18	5.0	2.8	1.8
3	0.21	41	106	4.3	13.4	18	2.0	69	22	33	24	8.4	5.1	1.7
4	0.25	40	111	4.5	17.0	20	2.1	69	31	46	30	10.5	5.8	1.8
5	0.20	186	75	14.0	18.4	19	6.3	2	454	693	818	30.2	10.6	2.8
6	0.25	188	79	14.8	22.2	22	6.6	2	634	892	1098	33.5	13.4	2.5

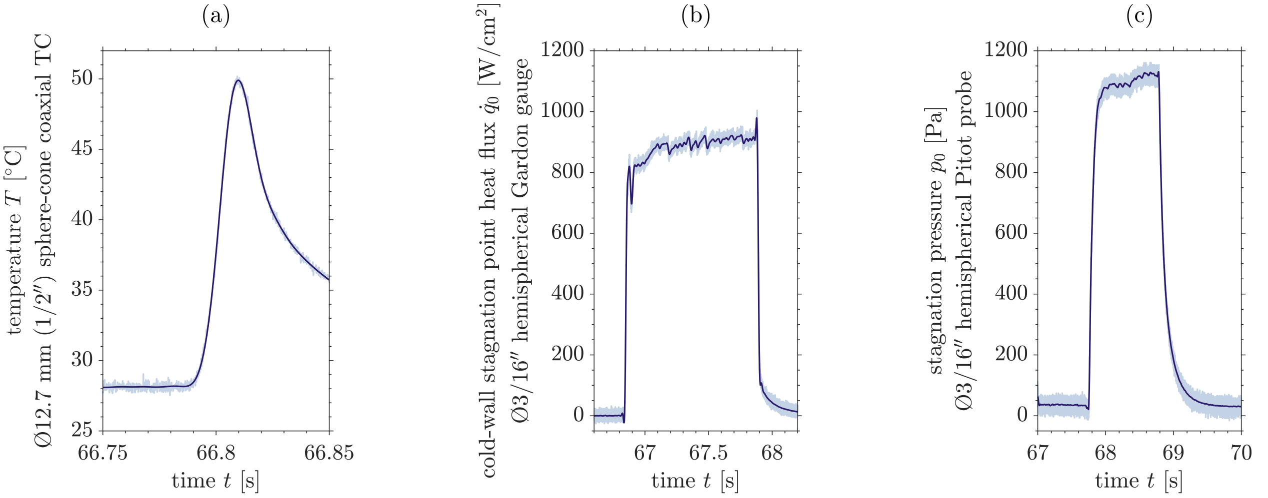

Fig. 2 Time-series for sensors mounted on trident sweep arm – raw signal (—) and filtered signal (—) for run 6: (a) temperature measured by a coaxial thermocouple calorimeter (⌀12.7 mm, 1/2'' sphere-cone) swept at a linear speed of 66.5 cm/s; (b) cold-wall stagnation point heat flux measured by a water-cooled Gardon gauge (⌀4.76 mm, 3/16'' hemispherical) during a 1-second dwell; (c) stagnation pressure measured by a water-cooled Pitot probe (⌀4.76 mm, 3/16'' hemispherical) during a 1-second dwell.

at the stagnation point. Additionally, chemical contributions to enthalpy may arise in high-enthalpy flows, though they are expected to be more significant under higher heat flux conditions and negligible under lower heat flux conditions. The average enthalpy ratio $h_0/\bar{h}$ for the runs performed is approximately 1.7 at the lower operating bounds (z = 69 mm, I_{set} = 40 A) and 2.7 at the upper operating bounds (z = 2 mm, I_{set} = 200 A).

Stagnation enthalpy values exceeding 30 MJ/kg and bulk enthalpy values above 12 MJ/kg are generally considered high, particularly when compared to other smaller-scale facilities, such as the 500 kW Tennessee High-Enthalpy Tunnel (TennHET), where $h_0 < 10$ MJ/kg and $\bar{h} < 5$ MJ/kg [37, 38]. However, similar values to those reported for the mARC II have been observed in higher-powered facilities, such as the 6 MW PWK at IRS Stuttgart (Germany) [39] and the 6 MW L2K and L3K facilities at DLR (Germany) [40].

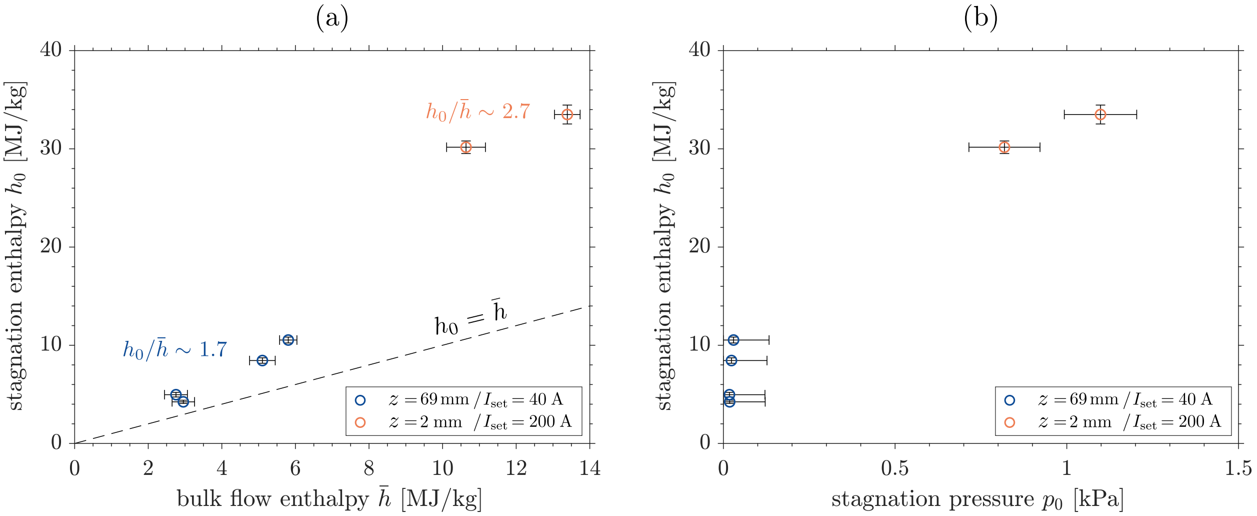

Fig. 3 Freestream flow enthalpy: (a) bulk flow enthalpy $\bar{h}$ vs. stagnation enthalpy h_0 ($\pm 1\sigma$) with average enthalpy ratios $h_0/\bar{h}$ noted; (b) flow stagnation properties – stagnation pressure p_0 vs. stagnation enthalpy h_0 ($\pm 1\sigma$).

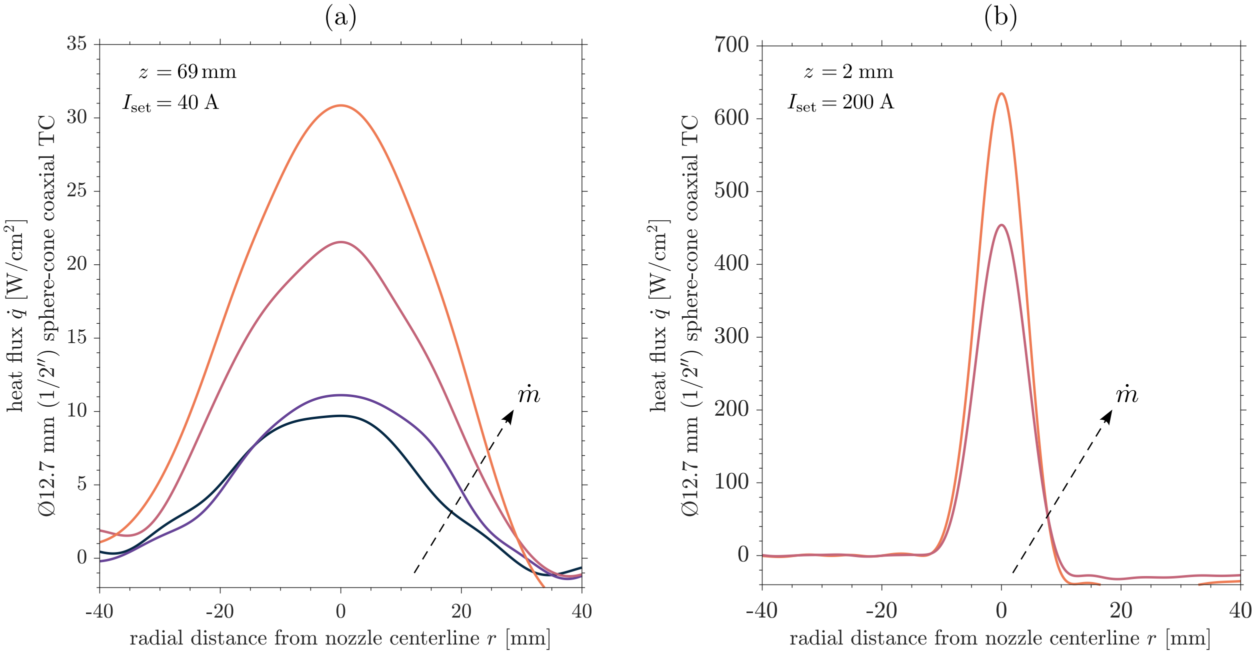

Fig. 4 Radial heat flux $\dot{q}$ measurements made using a coaxial thermocouple calorimeter (⌀12.7 mm, 1/2" sphere-cone) as a function of air mass flow rate $\dot{m}$: (a) set current of $I_{\mathrm{set}} = 40$ A with sensor at $z = 69$ mm from the nozzle exit plane for four different mass flow rates – 0.13 g/s (—), 0.14 g/s (—), 0.21 g/s (—), 0.25 g/s (—); (b) set current of $I_{\mathrm{set}} = 200$ A with sensor at $z = 2$ mm from the nozzle exit plane for two different air mass flow rates – 0.21 g/s (—), 0.25 g/s (—).

The high stagnation enthalpy values measured in the mARC II can be attributed to the efficient conversion of electrical energy from the arc into thermal energy within the plasma. The highest energy input occurs at the highest current setting ($I_{\mathrm{set}} = 200$ A), producing an energy-dense fluid that is expelled through a small nozzle throat into a controlled vacuum test box at high speeds. The pressure gradient between the arc column and the test box drives this rapid expulsion, allowing the fluid to reach stagnation almost immediately at the nozzle exit plane ($z = 2$ mm). This abrupt transition to stagnation condition explains the high values of stagnation enthalpy.

Figure 3b shows the stagnation properties of the freestream flow, measured by varying the air mass flow rate $\dot{m}$, set current I_{set}, and sensor distance from the nozzle z. At both $z = 2$ mm and $z = 69$ mm, stagnation enthalpy h_0 increases with stagnation pressure p_0, which aligns with theoretical expectations from inspection of Eq. (3). These high stagnation enthalpy values are partly due to the low stagnation pressures ($p_0 < 2.5$ kPa). In the previous iteration of the facility (mARC I), higher test box pressures resulted in stagnation pressures between 13 and 34 kPa, with corresponding lower stagnation enthalpies [7]. In the mARC II, the test box pressure can now be precisely controlled using a manual needle valve, offering flexibility in testing across different regions of the operating regime.

Finally, it is worth noting that stagnation enthalpy values derived from experimental heat flux measurements have been reported as being systematically low by Fletcher [34], even when careful attention is given to calorimeter surface cleanliness. As a result, the computed stagnation enthalpy values – and the resulting enthalpy ratios – may be slightly underestimated.

C. Radial heat flux profile $\dot{q}(r)$

In this section, we present the radial heat flux profiles of the freestream flow measured using a coaxial thermocouple calorimeter (⌀12.7 mm, 1/2" sphere-cone). Using the known motor speed and sweep arm length, the time-series heat flux signal from the coaxial thermocouple was converted into the radial coordinate system and shown in Figure 4.

Figure 4a presents data for the lowest set current of $I_{\mathrm{set}} = 40$ A at the farthest distance from the nozzle exit $z = 69$ mm. At the lowest mass flow rates (runs 1 and 2), the peak heat flux is around 10 W/cm^2, and the profile is nearly flat across approximately ±10 mm from the nozzle centerline. As the mass flow rate is increased, the profile begins to resemble that of the higher current condition shown in Fig. 4b, with a more pronounced peak and a sharper radial distribution.

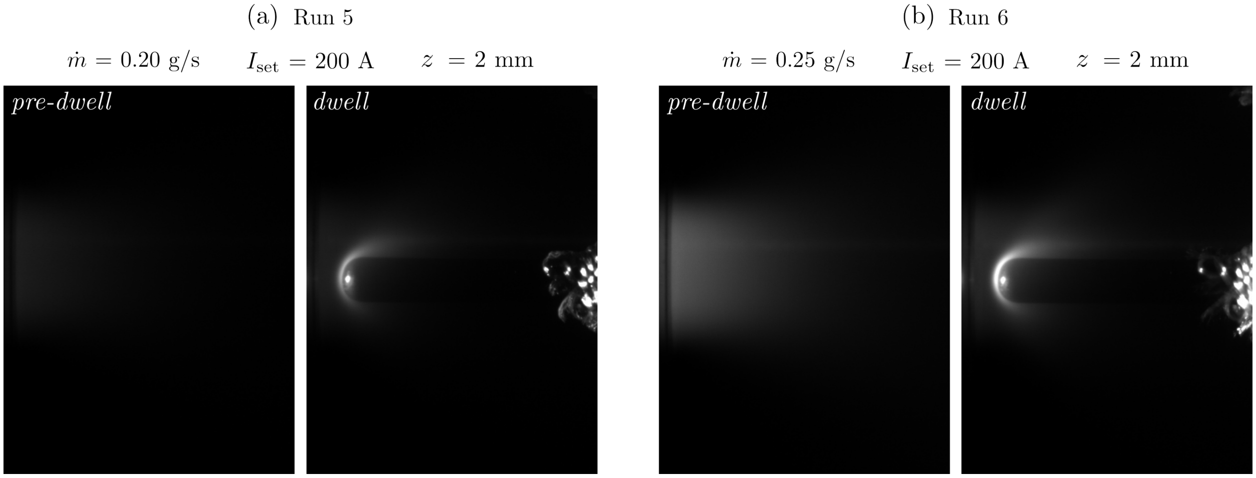

(a) Run 5

$\dot{m} = 0.20$ g/s $I_{\mathrm{set}} = 200$ A $z = 2$ mm

(b) Run 6

$\dot{m} = 0.25$ g/s $I_{\mathrm{set}} = 200$ A $z = 2$ mm

Fig. 5 Top view of the water-cooled Gardon gauge (⌀4.76 mm, 3/16" hemispherical) before and during the dwell (nozzle flow: left to right). Frames for (a) run 5 and (b) run 6 captured using a monochrome Chronos 1.4 camera (780±5 nm bandpass filter, 30 fps, 7.5 ms exposure, $f/11$, $f = 106$ mm, no gain, linear brightness encoding).

Figure 4b presents data for the highest set current $I_{\mathrm{set}} = 200$ A at the closest distance from the nozzle exit $z = 2$ mm. The heat flux profile here is much clearer and more defined than for $I_{\mathrm{set}} = 40$ A. The flow in the nozzle geometry is expected to be laminar, and since these measurements were taken immediately after the nozzle exit ($z = 2$ mm), the flow exhibits a parabolic profile typical of laminar flow. This parabolic shape is less evident in Fig. 4a since at $z = 69$ mm from the nozzle exit the flow has already expanded. The radial profiles in Fig. 4b also show a sharper peak compared to those in Fig. 4a, which can be attributed to two factors: first, the flow is confined at the nozzle exit and has no room to expand, and second, the 200 A condition generates a larger pressure gradient between the arc-heater column and the test box (see Table 2), resulting in much higher centerline velocities than at 40 A.

D. Imaging

An initial visual representation of the freestream flow structure and its interaction with the sensors can be obtained by analyzing data captured by the Chronos camera. Figure 5 presents four still frames before and during the 1-second dwell of the Gardon gauge, with the sensor tip positioned at $z = 2$ mm from the nozzle exit plane (runs 5 and 6). Since a 780±5 nm bandpass filter was used, the brightness of the images corresponds to flow regions emitting radiation from the 777 nm atomic oxygen triplet lines as well as areas where materials, such as Refrasil, thermally radiate due to heating by the high-temperature flow. Based on this, the bow shock upstream of the Gardon gauge is clearly visible in both runs during the sensor dwell. Prior to the dwell, atomic oxygen seems concentrated in the core of the underexpanded flow structure (Fig. 5b). Since both conditions used the same camera settings, it can be inferred that run 6, with a higher flow rate at the same current setting, produced a freestream flow that emitted more atomic oxygen than run 5 (Fig. 5a).

E. Operating envelope (p_0 vs. $\dot{q}_0$)

In our previous work, we demonstrated how the upgraded vacuum system extended the lower end of the heat flux regime. In this section, we present an initial operating envelope, commonly defined in the arc-jet community by plotting the measured stagnation pressure p_0 and cold-wall stagnation point heat flux $\dot{q}_0$, ensuring that the specific calorimeter probe geometry is clearly described in the figure axis [12]. In our case, the water-cooled Gardon gauge (⌀4.76 mm, 3/16" hemispherical) is currently the reference calorimeter for the mARC II facility. The average stagnation point heat flux and stagnation pressure are calculated over the steady-state dwell time, as shown in Fig. 2.

Figure 6 presents the operating envelope, illustrating the impact of the facility upgrades on the key variables defining the envelope by comparing the data collected in this study with previous data from mARC II (prior to the vacuum system upgrades) [11] and mARC I [7]. The reduced test box pressure during test conditions not only enables testing at lower heat fluxes, but also enables testing at lower stagnation pressures. This added capability enhances testing flexibility by introducing an additional control variable. Specifically, we can now also adjust the operating point within the regime

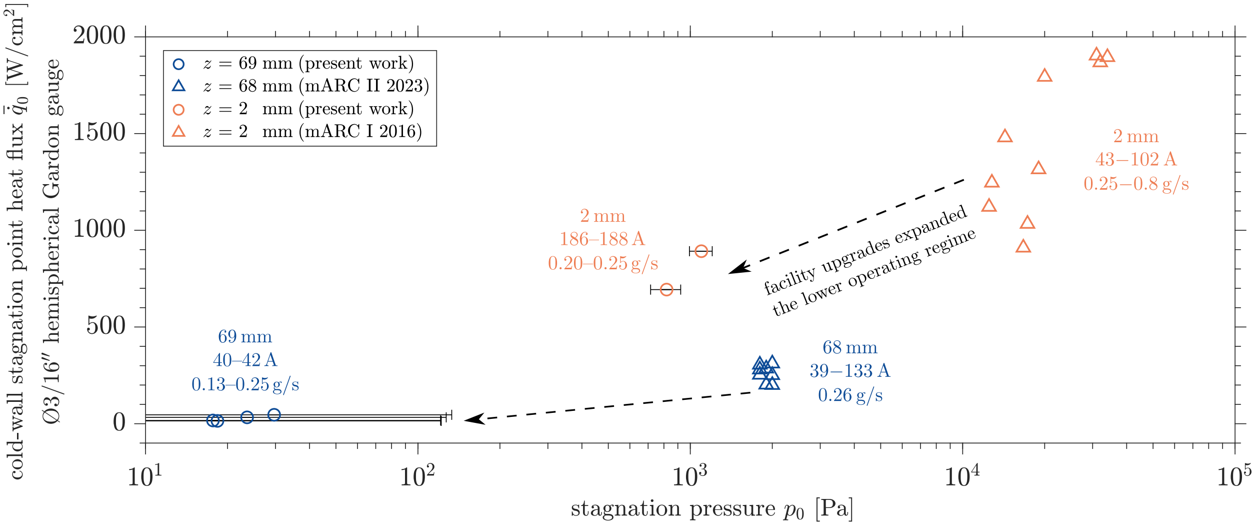

Fig. 6 Operating envelope for the upgraded mARC II arc-jet facility compared to previous mARC iterations.

by increasing the test box pressure, which can be achieved by bleeding air into the test box using a manual valve. This adjustment would affect the nozzle pressure ratio, alter the nozzle flow structure, and consequently influence stagnation heat flux and pressure. Overall, the vacuum system upgrades have significantly expanded the mARC II facility's lower operating regime, enabling consistent and reliable operation at lower test box pressures.

IV. Conclusions

This work presents initial data evaluating the impact of the vacuum system upgrades on the operating envelope of the mARC II facility, while also demonstrating several enhanced measurement capabilities. These upgrades allowed for the improved measurement of bulk flow enthalpy cooling losses and enabled the first-time characterization of the radial heat flux profile using a swept coaxial thermocouple calorimeter (⌀12.7 mm, 1/2" sphere-cone), with corrections for two-dimensional heat conduction effects. While bulk flow measurements had been previously published, this study compares bulk flow enthalpy and centerline enthalpy in the mARC II for the first time. Additionally, spectrally-filtered imaging captured the freestream flow as well as the bow shock upstream of dwelled sensors.

In our earlier work, we showed that the upgraded vacuum system extended the lower end of the heat flux regime. In this study, six data points for the operating regime are presented from cold-wall stagnation point heat flux measurements made using a water-cooled Gardon gauge (⌀4.76 mm, 3/16" hemispherical) and stagnation pressure measurements made using a water-cooled Pitot probe (⌀4.76 mm, 3/16" hemispherical). This study further demonstrates that the reduced test box pressure not only allows for testing at lower heat fluxes but also enables testing at lower stagnation pressures. These capabilities position mARC II as a key potential facilitator in the development of novel Thermal Protection System (TPS) technologies, particularly those with testing requirements at the lower end of the heat flux and stagnation pressure spectrum.

V. Future work

Ongoing efforts are focused on completing the characterization of the mARC II operating envelope for air flows, including the effects of current, flow rate, and axial location. This will define the bounds of the operating regime for arc stability and identify optimal testing conditions. Numerical simulations will complement the experimental data, enabling a more comprehensive analysis and comparison with both intrusive and non-intrusive measurements. Optical diagnostics are being implemented, with preliminary data already being analyzed to enhance our understanding of the freestream flow structure and composition. Additional imaging capabilities have been integrated into the facility and will be discussed in upcoming work.

A detailed uncertainty quantification for heat flux measurements is underway and a methodology for scaling of heat fluxes to correct for calorimeter geometry of varying sizes and shapes is under development. Additionally, we will explore the possibility of using transducers with reduced full-scale outputs to reduce measurement uncertainty at low stagnation pressures. This will involve evaluating various transducer models tailored to specific regions of the operating envelope.

Lastly, we aim to to support the testing and development of thermal protection system (TPS) materials in the near future. This would involve examining the performance of materials within the mARC II operating envelope, offering valuable insights for material development and demonstrating mARC II's potential as a material testing platform.

Acknowledgments

J. Rodrigues is the recipient of a NASA Postdoctoral Program (NPP) research fellowship at NASA Ames Research Center, administered by Oak Ridge Associated Universities (ORAU) under contract with NASA. S. Colom is supported through the NASA NNA15BB15C contract. R. Chung and J. Hartman are supported through the NASA 80ARC022DA011 contract. The authors would like to thank Joseph Mach and Tomomi Oishi for supporting the calibration of the optical temperature sensors.

References

[1] Fu, J., Olivares, R., Oishi, T., Martinez, E., and Gorbunov, S., "XJet: A Small-Scale Aerothermal Test Environment for Instrumentation," *44th AIAA Aerospace Sciences Meeting and Exhibit*, American Institute of Aeronautics and Astronautics, Reston, Virigina, 2006, pp. 16064–16072.

[2] Beck, R. A., White, S., Arnold, J., Fan, W., Stackpoole, M., Agrawal, P., and Coughlin, S., "Overview of Initial Development of Flexible Ablators for Hypersonic Inflatable Aerodynamic Decelerators," *21st AIAA Aerodynamic Decelerator Systems Technology Conference and Seminar*, American Institute of Aeronautics and Astronautics, Reston, Virginia, 2011, pp. 1–16.

[3] Fan, W., Thornton, J., Chavez-Garcia, J., Beck, R., and Ghandehari, E., "Charring Behavior of Lightweight Silicone-based Ablators," *43rd AIAA Thermophysics Conference*, American Institute of Aeronautics and Astronautics, Reston, Virginia, 2012, pp. 1–11.

[4] White, S., "Effects of Laser Wavelength on Ablator Testing," *38th Annual Conference on Composites, Materials and Structures*, No. ARC-E-DAA-TN12788, 2014.

[5] Codron, D. A., and Nawaz, A., "Radial Profiles of Plasma Electron Characteristics in a 30 kW Arc Jet," *44th AIAA Plasmadynamics and Lasers Conference*, American Institute of Aeronautics and Astronautics, Reston, Virginia, 2013, pp. 1–12.

[6] Codron, D. A., Cruden, B. A., and Ho, T., "Emission Spectroscopy Characterization of Thermal Protection System Materials in Arc-Heated Flows," *45th AIAA Plasmadynamics and Lasers Conference*, American Institute of Aeronautics and Astronautics, Reston, Virginia, 2014, p. 2112.

[7] Nawaz, A., Ho, T. S., Philippidis, D., MacDonald, M., McGlaughlin, M. S., and Driver, D. M., "Baseline characterization of the 30 kW miniature arc jet facility mARC at NASA Ames," *32nd AIAA Aerodynamic Measurement Technology and Ground Testing Conference*, American Institute of Aeronautics and Astronautics, Reston, Virginia, 2016, pp. 1–24.

[8] MacDonald, M. E., Philippidis, D., Ho, T., Haw, M., Hartman, J., and McGlaughlin, M., "Build-up of the second-generation 30 kW miniature arc jet (mARC II) at NASA Ames Research Center," *AIAA Aviation 2019 FORUM*, American Institute of Aeronautics and Astronautics, Reston, Virginia, 2019, pp. 1–12.

[9] MacDonald, M. E., Philippidis, D., Haw, M., Schickele, D., Luis, D., Hartman, J., and McGlaughlin, M., "Initial Characterization of the 30 kW Miniature Arc Jet (mARC II) at NASA Ames Research Center," *AIAA AVIATION 2020 FORUM*, American Institute of Aeronautics and Astronautics, Reston, Virginia, 2020, pp. 1–15.

[10] Luís, D., and MacDonald, M. E., "Emission spectroscopy characterization of electrode species in the freestream flow at the NASA Ames miniature Arc Jet II facility," *Journal of Quantitative Spectroscopy and Radiative Transfer*, Vol. 272, 2021, p. 107752.

[11] MacDonald, M. E., Haw, M. A., Martinez, R., Colom, S., Rodrigues, J., Chung, R., and Hartman, J., "Characterizing Heat Flux in the miniature Arc jet Research Chamber (mARC II)," *AIAA AVIATION 2023 Forum*, American Institute of Aeronautics and Astronautics, San Diego, California, 2023, pp. 1–9.

[12] Terrazas-Salinas, I., "Test Planning Guide for NASA Ames Research Center Arc Jet Complex and Range Complex [A029-9701-XM3 Rev. J – July 28, 2022]," NASA Ames Research Center, 2022.

[13] Rodrigues, J., Macdonald, M. E., Haw, M. A., Martinez, R., Philippidis, D., Colom, S., Chung, R., and Hartman, J., "Defining the Operational Envelope for Air Flows in the miniature Arc jet Research Chamber (mARC II)," *AIAA AVIATION FORUM AND ASCEND 2024*, AIAA, Las Vegas, Nevada, 2024.

[14] Franquet, E., Perrier, V., Gibout, S., and Bruel, P., "Free underexpanded jets in a quiescent medium: A review," *Progress in Aerospace Sciences*, Vol. 77, 2015, pp. 25–53.

[15] Duthil, P., "Material Properties at Low Temperature," *CERN Yellow Report CERN-2014-005*, 2014, pp. 77–95.

[16] Minneci, R. P., Lass, E. A., Bunn, J. R., Choo, H., and Rawn, C. J., "Copper-based alloys for structural high-heat-flux applications: a review of development, properties, and performance of Cu-rich Cu–Cr–Nb alloys," *International Materials Reviews*, Vol. 66, No. 6, 2021, pp. 394–425.

[17] Preston-Thomas, H., "The International Temperature Scale of 1990 (ITS-90)," *Metrologia*, Vol. 27, No. 107, 1990, pp. 3–10.

[18] Driver, D. M., Philippidis, D., and Terrazas-Salinas, I., "Uncertainty Analysis of Coaxial Thermocouple Calorimeters used in Arc Jets," *2018 Joint Thermophysics and Heat Transfer Conference*, American Institute of Aeronautics and Astronautics, Reston, Virginia, 2018, p. 3770.

[19] Moore, C. E., "National Standard Reference Data System – National Bureau of Standards 3, Section 7 (U.S. Department of Commerce)," , 1975.

[20] Pearse, R. W. B., and Gaydon, A. G., *The identification of molecular spectra*, 4th ed., John Wiley & Sons, 1976.

[21] ASTM International, "Standard Practice for Measuring Plasma Arc Gas Enthalpy by Energy Balance [ASTM E341–08]," ASTM International, 2020.

[22] Hightower, T. M., Balboni, J. A., MacDonald, C. L., Anderson, K. F., and Martinez, E. R., "Enthalpy by energy balance for aerodynamic heating facility at NASA Ames Research Center Arc Jet Complex," *48th International Instrumentation Symposium*, 2002, pp. 1–13.

[23] International Institute of Refrigeration, *Thermophysical Properties of Liquid Secondary Refrigerants: Tables and Diagrams for the Refrigeration Industry*, 1997.

[24] Kawaizumi, F., Otake, T., Nomura, H., and Miyahara, Y., "Heat Capacities of Aqueous Solutions of Ethylene Glycol, Propylene Glycol and 1,3-Butanediol," *Journal of the Chemical Society of Japan*, Vol. 10, 1972, pp. 1773–1776.

[25] Melinder, ., "Thermophysical Properties of Aqueous Solutions Used as Secondary Working Fluids," Ph.D. thesis, Royal Institute of Technology, KTH, Stockholm, Sweden, 2007.

[26] Zoby, E. V., "Empirical stagnation-point heat-transfer relation in several gas mixtures at high enthalpy levels (NASA TN D-4799)," NASA Langley Research Center, Hampton, VA, USA, 1968.

[27] Fay, J. A., and Riddell, F. R., "Theory of Stagnation Point Heat Transfer in Dissociated Air," *Journal of the Aerospace Sciences*, Vol. 25, No. 2, 1958, pp. 73–85.

[28] ASTM International, "Standard Test Method for Calculation of Stagnation Enthalpy from Heat Transfer Theory and Experimental Measurements of Stagnation-Point Heat Transfer and Pressure [ASTM E637–22]," ASTM International, 2022.

[29] Zoby, E. V., and Sullivan, E. M., "Effects of Corner Radius on Stagnation-Point Velocity Gradients on Blunt Axisymmetric Bodies," *Journal of Spacecraft and Rockets*, Vol. 3, No. 10, 1966, pp. 1567–1567.

[30] Zoby, E. V., and Sullivan, E. M., "Effects of corner radius on stagnation-point velocity gradients on blunt axisymmetric bodies (NASA-TM-X-1067)," NASA Langley Research Center, 1966.

[31] Pope, R. B., "Stagnation-point convective heat transfer in frozen boundary layers." *AIAA Journal*, Vol. 6, No. 4, 1968, pp. 619–626.

[32] Pope, R. B., "Measurements of enthalpy in low-density arc- heated flows," *AIAA Journal*, Vol. 6, No. 1, 1968, pp. 103–110.

[33] Jorgensen, L. H., and Redmond, R. J., "Charts for equilibrium flow properties of carbon dioxide in hypervelocity nozzles [SP-3015]," NASA Ames Research Center, 1964.

[34] Fletcher, D. G., “Measurement Techniques for High Enthalpy and Plasma Flows: Measurement Requirements for Improved Modeling of Arcjet Facility Flows,” *RTO AVT Course — Measurement Techniques for High Enthalpy and Plasma Flows*, NATO Research and Technology Organization, NATO Research and Technology Organization, Rhode-Saint-Genèse, Belgium, 1999, pp. 1–27.

[35] Lord Rayleigh, “Aerial plane waves of finite amplitude,” *Proc. R. Soc. Lond. A*, Vol. 84, No. 570, 1910.

[36] Shapiro, A. H., *The Dynamics and Thermodynamics of Compressible Fluid Flow*, Ronald Press, New York, 1953.

[37] Baccarella, D., and Samuels, K. E., “Testing and Characterization of the University of Tennessee High-Enthalpy Tunnel,” *AIAA SCITECH 2023 Forum*, American Institute of Aeronautics and Astronautics, Reston, Virginia, 2023.

[38] Baccarella, D., and Samuels, K., “Spectroscopic Characterization of a Hypersonic Arcjet Flow,” *AIAA AVIATION 2023 Forum*, American Institute of Aeronautics and Astronautics, Reston, Virginia, 2023, pp. 1–11.

[39] Loehle, S., Zander, F., Eberhart, M., Hermann, T., Meindl, A., Massuti-Ballester, B., Leiser, D., Hufgard, F., Pagan, A. S., Herdrich, G., and Fasoulas, S., “Assessment of high enthalpy flow conditions for re-entry aerothermodynamics in the plasma wind tunnel facilities at IRS,” *CEAS Space Journal*, Vol. 14, No. 2, 2022, pp. 395–406.

[40] Esser, B., and Gülhan, A., “Flow field characterisation of DLR’s arc heated facilities L2K and L3K,” *Aerothermodynamics for space vehicles*, Vol. 426, 1999, p. 545.